An integrated-nanophotonics polarization beamsplitter with 2.4 × 2.4 μm² footprint

Bing Shen[1], Peng Wang[1], Randy Polson[2] and Rajesh Menon[1]*

We have designed, fabricated and characterized an integrated-nanophotonics polarization beamsplitter with a footprint of 2.4 × 2.4 μm², which is the smallest polarization beamsplitter ever demonstrated. A nonlinear optimization algorithm was used to design the device for λ_0 = 1,550 nm. The polarization beamsplitter and the input/output waveguides can be fabricated in a single lithography step. Here, we experimentally show an average transmission efficiency of greater than 70% (peak transmission efficiency of ~80%) and an extinction ratio greater than 10 dB within a bandwidth of 32 nm. Simulation results indicate that our device is tolerant to fabrication errors of up to ±20 nm in the device thickness. We also designed, fabricated and characterized a mode-converting polarization beamsplitter, which not only separates the two polarization states but also connects one multimode input waveguide to two single-mode output waveguides.

Silicon-on-insulator (SOI) is the main materials system used in integrated photonics because of the difference in refractive index between silicon and silicon dioxide. However, this feature results in strong birefringence, which leads to polarization-sensitive performance[1]. One solution to the problem is to compensate for polarization-mode dispersion, which requires a very challenging fabrication accuracy of 1 nm (ref. 2). A better solution is to use devices that process different polarization states separately. However, this requires an efficient and compact polarization beamsplitter (PBS). The working principle underpinning conventional PBS devices is based on either modal evolution[3,4] or interferometry. The latter typically include multimode interference couplers (MMIs)[5,6], directional couplers (DCs)[2,7–13] and Mach–Zehnder interferometers (MZIs)[14,15]. Among these, PBS devices based on DCs are preferred, because they generally provide the smallest footprint. DCs, in general, are composed of silicon waveguides[2,10], photonic crystals[11,13], slot waveguides[9] or a combination of a silicon channel and slot waveguide[7]. For DCs composed of silicon channels, Fukuda and colleagues have demonstrated a PBS with dimensions of 7 μm × 16 μm that exhibited an extinction ratio of 15 dB (ref. 2). However, the fabrication precision required for the waveguides and the gap between the waveguides is very stringent due to its underlying phase-matching principle. In addition, the fundamentally small evanescent coupling prevents it from achieving large extinction ratios. Photonic-crystal-based DCs are a plausible alternative for compact PBS devices[11,13], but light coupling between the commonly used silicon waveguides and photonic-crystal waveguides is challenging. DCs based on slot waveguides[9] or the combination of slot waveguides and silicon channels[7] could enable the fabrication of smaller devices due to the tighter mode confinement within the slot. Combining a slot waveguide and silicon channels, Dai and co-workers designed a PBS with a length of 6.9 μm and an extinction ratio larger than 10 dB (ref. 7). Again, strict requirements for the precision of fabrication are

inevitable due to its underlying phase-matching principle. Recently, Guan and colleagues proposed a DC-based PBS composed of a hybrid plasmonic waveguide and a silicon nanowire[12]. This device has dimensions of 1.9 μm × 3.7 μm, but the incorporation of metal creates significant parasitic absorption losses and renders the process complementary metal–oxide–semiconductor (CMOS) incompatible.

In contrast to previous device designs, we make use of the concept of free-form metamaterials in our PBS device. Allowing the geometry of the metamaterials to be freely optimized enables devices that can be highly functional, but which occupy a small footprint[16–18]. Nanopatterning enables one to engineer the refractive index in space at a deep sub-wavelength scale. In this way, devices that achieve high-efficiency mode conversion in an extremely small area become feasible. Furthermore, these devices tend to rely on the coupling between a number of resonant nanophotonic modes, which promotes robustness to fabrication errors, as discussed later. Here, we have designed, fabricated and characterized an ultra-compact PBS with a footprint of only 2.4 × 2.4 μm² for a design wavelength of 1.55 μm and an extinction ratio larger than 12 dB. As far as we know, this is the smallest-area PBS ever demonstrated. We refer to this device as a nanophotonic PBS (see Fig. 1a for its geometry). The PBS is patterned on an SOI substrate, in which the thicknesses of the silicon and oxide layers are 0.3 μm and 3 μm, respectively. Note that the device is also CMOS-compatible.

The device is composed of 20 × 20 pixels. One pixel is in the shape of a square, with sides of 120 nm, giving a device footprint of 2.4 × 2.4 μm². Unpolarized light, excited at the far end of the left input waveguide (Fig. 1a), illuminates the PBS. Transverse magnetic (TM) and transverse electric (TE) components of the input light are coupled into the top and bottom output waveguides with calculated efficiencies of 89% and 81%, respectively. The simulated intensity distributions for both polarizations are shown in Fig. 1b,c. From the simulations we can clearly see that the incident light generates resonant modes within the nanophotonic device that are polarization-dependent (see Supplementary Movie 1 for an animation). These guided resonant modes interact in such a manner as to satisfy the phase-matching conditions for the respective polarizations at the corresponding output waveguides. As a result, polarization splitting is achieved. In the device geometry in Fig. 1a, silicon is shown in black and the absence of silicon (air) as white. The device is designed such that the thickness of the silicon layer in the nanophotonic region is the same as that in the waveguides, that is, 300 nm. This implies that our design can be fabricated in a single lithography step along with the waveguides.

The nanophotonic PBS was designed using a nonlinear search algorithm that we refer to as 'direct-binary search' (DBS). Previously, we have applied different versions of the DBS algorithm to design solar concentrators[19], free-space polarizers[20], integrated-photonic

---

[1]Department of Electrical and Computer Engineering, University of Utah, Salt Lake City, Utah 84112, USA. [2]Utah Nanofabrication Facility, University of Utah, Salt Lake City, Utah 84112, USA. *e-mail: rmenon@eng.utah.edu
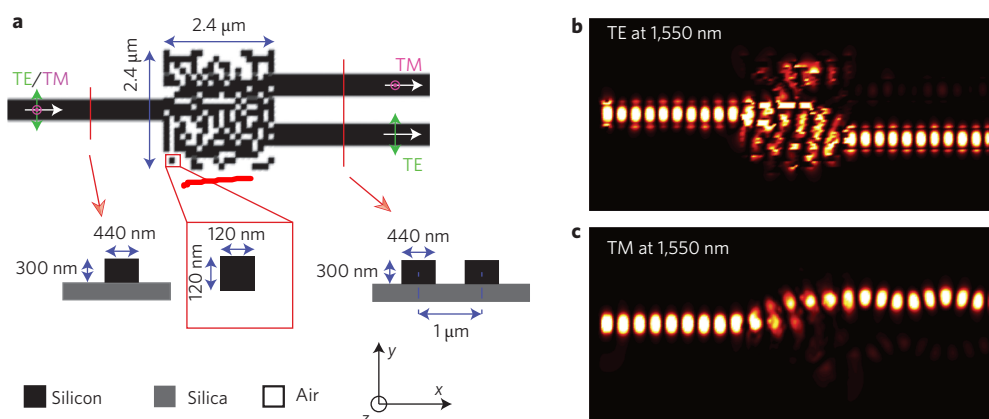
Figure 1 | The nanophotonic polarization beamsplitter. a, Geometry of the device. **b,c**, Simulated steady-state intensity distributions for TE (**b**) and TM (**c**) polarized light at the design wavelength of 1,550 nm (Supplementary Movie 1). TE is polarized in-plane and perpendicular to the propagation direction, as illustrated by the green arrows in **a**, and TM is polarized out-of-plane, as illustrated by red circles in **a**.

devices[17] and nanostructures for enhanced light absorption[21,22], as well as to enable computational microscopy[23]. The device under consideration is discretized into hundreds of 120 nm × 120 nm silicon/air pillars, which we call 'pixels'. Because the device has dimensions of 2.4 μm × 2.4 μm, there are 20 × 20 pixels. Each such pixel can occupy two states: silicon or air. A randomly chosen pixel is first perturbed so as to switch its state, then a figure-of-merit (FOM) is calculated. The FOM is defined as the average transmission efficiency for TE and TM polarization states. The pixel state is retained if the FOM is improved. If not, the perturbation is reversed and the algorithm proceeds to the next pixel. A single iteration comprises such inspection of all pixels. The iterations continue until the FOM does not improve further. The algorithm seamlessly accounts for the limitations of the fabrication technologies because of the discrete pixels. Specifically, the fabrication process determines the size of the smallest feature, which, in our device, is the pixel. Although the computational cost of this step is high, we have previously reported a variety of approaches to parallelize and increase the computational efficiency[17]. In general, it took about 140 h to design one device. The electromagnetic fields within the device were simulated using a finite-difference time-domain (FDTD) method[24]. (See Supplementary Section 1 for a detailed description of the design process.)

As mentioned already, the device was patterned in the top silicon layer (thickness, 300 nm) of an SOI substrate. In principle, only one patterning step is required for the waveguides and the nanophotonic PBS, because their etch depths are the same. However, because we do not have access to high-resolution optical-projection lithography, we opted for a two-step process. Optical patterning was first used to define all features down to a size of 3 μm. Second, focused-ion-beam lithography was used to define all the smaller features. Alignment marks were used to ensure that the patterns defined by the two

lithographic steps were aligned with one another. Further details of the fabrication process are provided in Supplementary Section 6. Reference devices that included the same tapers as the PBS devices for normalization, as well as an on-chip polarizer for polarization state alignment, were also fabricated on the same substrate.

A scanning electron micrograph of the fabricated device is shown in Fig. 2a. Light was input and output via butt-coupling of lensed fibres to multimode waveguides (Fig. 2b). To increase the coupling efficiency we incorporated tapers (4 μm length) between all single-mode waveguides and the multimode waveguides (width, 3 μm)[25]. The fibres used in the experiment were standard single-mode lensed fibres. Polarization controllers (PC1 and PC2) were first calibrated using the on-chip polarizer (see Supplementary Section 4 for details of the on-chip polarizer). The entire output path within the dotted frame in Fig. 2b was first bypassed by connecting the output lensed fibre to the detector, and the on-chip polarizer was aligned. By adjusting PC1 and monitoring the output power, the input polarization state was set. The input lensed fibre was then moved to illuminate a straight waveguide, and the output path within the dotted frame was connected. The alignment between the output polarization plane and the polarizer was achieved by adjusting PC2. The polarization components of the output light could be selected by rotating the polarizer.

The experimental and simulated transmission efficiency and extinction ratio as a function of input wavelength are shown in Fig. 3a,b, respectively. The experimental data are normalized to those for a straight waveguide with the same tapers (Supplementary Section 4). The measured values consistently follow the simulated curves. The decrease in measured efficiencies can be primarily attributed to small errors introduced during fabrication, which include device thickness errors and line-edge roughness. The latter can cause out-of-plane scattering, which will
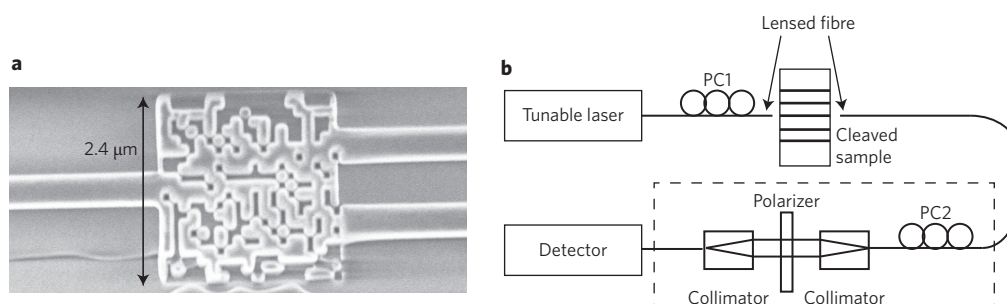

Figure 2 | Experiment. a, Scanning electron micrograph of the fabricated device. **b**, Measurement system set-up.
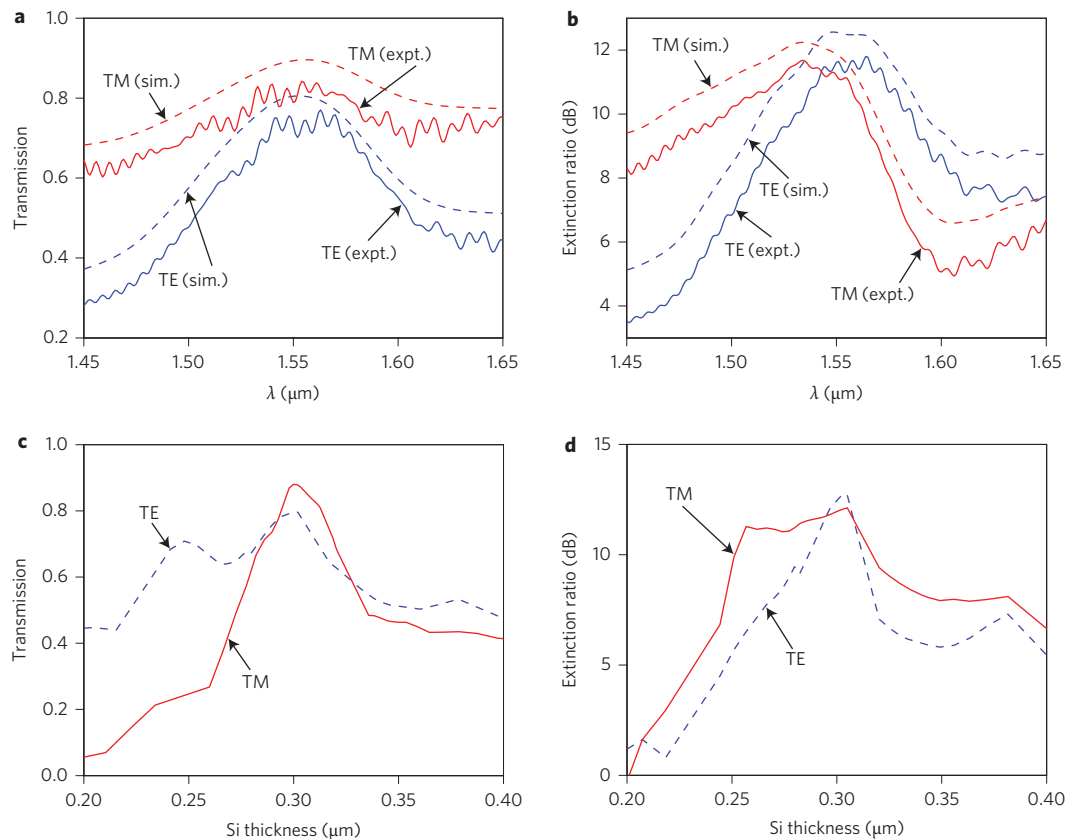
Figure 3 | Experimental and simulated performance of the nanophotonic PBS. a,b, Measured and simulated transmission efficiencies (**a**) and extinction ratios (**b**) of the PBS for both TE and TM polarization. Measured (expt.) and simulated (sim.) data are shown using solid and dashed lines, respectively. **c,d**, Simulated transmission efficiencies (**c**) and extinction ratios (**d**) as a function of device (silicon) thickness. For all figures, TE and TM polarizations are shown in blue and red, respectively.

reduce overall efficiencies. Improved fabrication processes can significantly reduce these effects. We believe that coherent interactions between light reflected from the lensed fibre and that from the waveguides cause the ripples in the measured spectra. We measured TE and TM coupling efficiencies of 71% and 80% at the design wavelength (1.55 μm), respectively. The measured TE and TM extinction ratios at the design wavelengths are 11.8 dB and 11.1 dB, respectively.

The operational bandwidth of our device, where the transmission efficiency is within 1 dB of the peak value, is 83 nm (1,510–1,593 nm) (Fig. 3a). Such a large operating bandwidth is possible because the polarization-selection effect is the cumulative effect of a number of guided-mode resonances (rather than a single resonance).

To elucidate the tolerance of our device to small changes in device geometry, we simulated the impact of varying the top silicon thickness on device performance. The results for transmission efficiency and extinction ratio are illustrated in Fig. 3c,d, respectively. If the extinction ratio is allowed to fall 3 dB from the peak value, the devices can tolerate a variation in top silicon thickness of up to ±20 nm.

We also simulated the instantaneous field distributions within the PBS as a function of time (see Supplementary Movie 1 for an animation). Both TE and TM modes in the input waveguide illuminate the PBS. The nanophotonic device is composed of geometries that are much smaller than the wavelength, so the excited modes are evanescent. However, power is coupled between the evanescent modes due to the close spacing. This results in multiple resonant modes that transfer power in a highly polarization-sensitive manner. Our design methodology essentially encourages the power transfer of one polarization into one waveguide, while the power in the orthogonal polarization is transferred to the second waveguide.

A closer look at the mode evolution with time (Supplementary Movie 1) shows that different mechanisms are responsible for guiding light in the two polarization states. For TE light (light polarized in-plane and vertical to the direction of light propagation), power is confined in the air gap between adjacent nanopillars and the slot–waveguide effect dominates due to boundary conditions. The silicon pillars actually act as the cladding layer and the air gaps act as the core layer to guide TE light (Supplementary Movie 1). The opposite holds true for TM light (light polarized out-of-plane), in that the air gaps act as the cladding layer and the silicon pillars act as the core layer to guide TM light (Supplementary Movie 1). The complementary guiding mechanisms are employed by the optimization algorithm to design the PBS to direct different polarization states to their corresponding output waveguides.

Complex nanophotonic structures allow one to design a single device that can implement multiple functions. To illustrate this concept, we designed, fabricated and characterized a device that not only coverts light from a multimode waveguide to a single-mode waveguide, but also splits the two polarizations. The device geometry is illustrated in Fig. 4a, and a scanning electron micrograph of the fabricated device is shown in Fig. 4b. A 3-μm-wide multimode waveguide is used as the input, and the output comprises two single-mode (440-nm-wide) waveguides. Due to the significant dimension mismatch between the input and output waveguides, mode conversion is required, which is typically achieved with a very long (hundreds of micrometres) adiabatic taper[16,26]. For our device, however, polarization splitting and mode conversion are
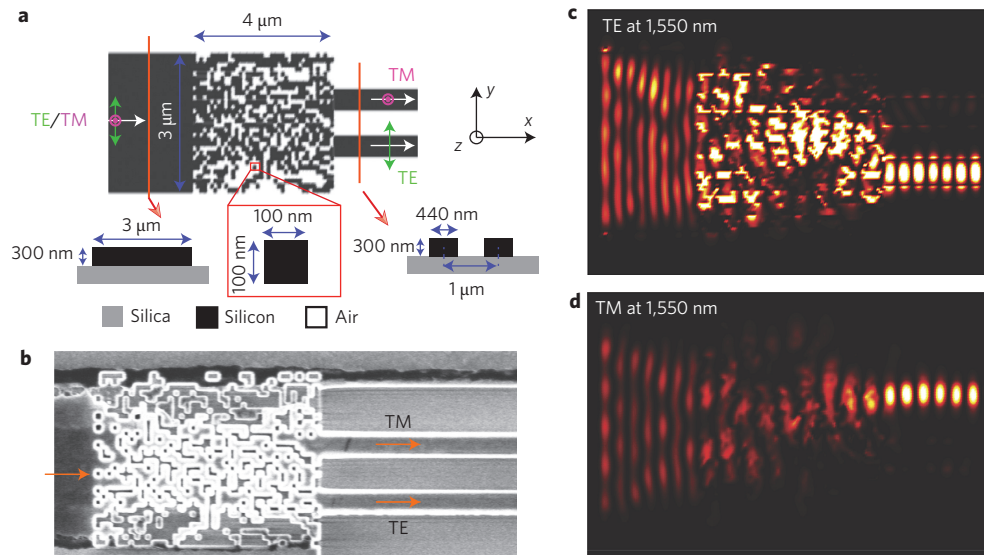
Figure 4 | Mode-converting PBS. a,b, Configuration (**a**) and scanning electron micrograph (**b**) of the mode-converting PBS. **c,d**, Intensity distributions for TE (**c**) and TM (**d**) polarized light at 1,550 nm (Supplementary Movie 2).
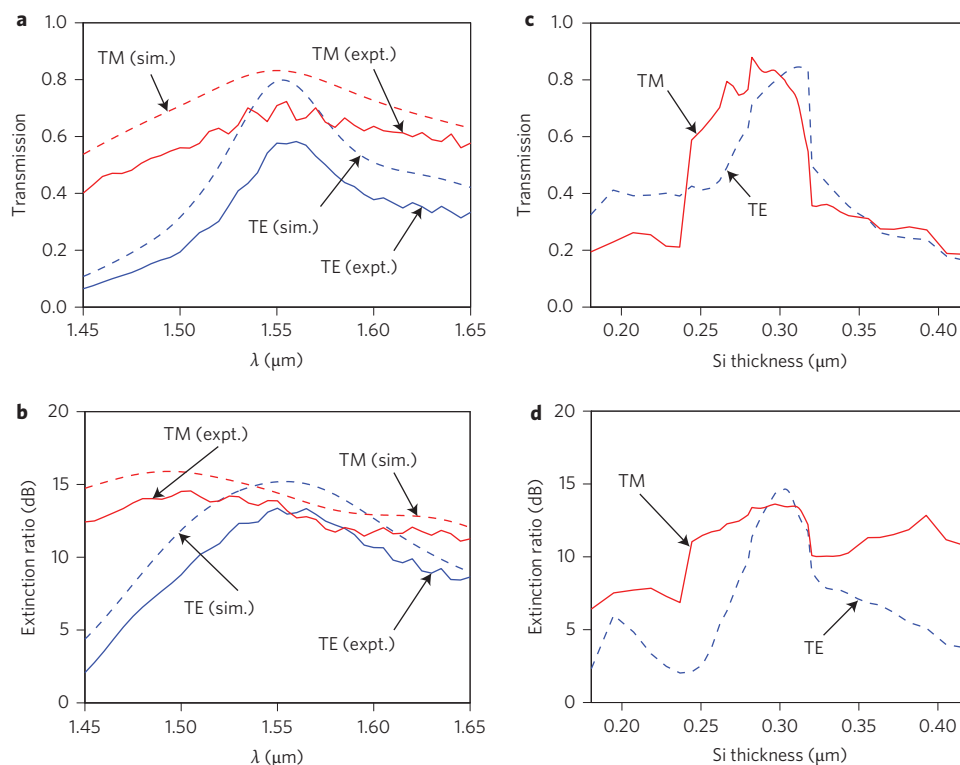

Figure 5 | Experimental and simulated performance of the nanophotonic mode-converting PBS. a, Simulated and measured transmission efficiencies as a function of wavelength. **b**, Simulated and measured extinction ratio as a function of wavelength. TE and TM are denoted by blue and red lines, and dashed and solid lines represent the corresponding simulation and experimental efficiencies. **c,d**, Simulated transmission efficiency (**c**) and extinction ratio (**d**) as a function of silicon thickness.

achieved simultaneously. The simulated intensity distributions for the two polarization states are summarized in Fig. 4c,d.

The simulated and measured properties of the device are summarized in Fig. 5a,b. The simulated transmission efficiencies at the design wavelength (1.55 μm) for TE and TM modes are calculated as 80% and 83%, respectively. The corresponding simulated extinction ratios are 15.2 dB and 14.4 dB for TE and TM. The measured transmission-efficiency and extinction-ratio spectra are

lower than the simulated spectra, but substantially agree. The measured peak transmission efficiencies for TE and TM are 58% and 71%, and the measured extinction ratios are 13.88 dB and 13.77 dB, respectively. The measured efficiencies are lower than expected primarily due to errors in alignment between the PBS and the waveguides, as discussed in Supplementary Section 3. With a single-step lithography process, such alignment will be unnecessary and these errors should not manifest. Note that both

polarization separation and mode conversion are achieved within the 4 μm × 3 μm device area. An animation showing the field distribution as a function of time is provided in Supplementary Movie 2.

The impact of device geometry errors was also simulated to evaluate the tolerance of our design, and the results are summarized in Fig. 5c,d. Specifically, we varied the device (silicon layer) thickness and then evaluated its performance. The simulations indicate that if the extinction ratio is allowed to fall 3 dB from the peak, then the silicon layer thickness can vary by as much as ±17 nm.

In conclusion, we have designed an ultra-compact integrated nanophotonic PBS using a nonlinear search algorithm based on direct-binary search. Our design methodology readily incorporates the limitations of fabrication, so our devices tend to be robust and can easily be made compatible with CMOS fabrication processes. We have characterized the devices and experimentally demonstrated TE and TM transmission efficiencies of 71% and 80%, respectively, with corresponding extinction ratios of 11.8 dB and 11.1 dB. The $2.4 \times 2.4\ \mu m^2$ footprint of our PBS makes it the smallest integrated PBS demonstrated to date[12]. Furthermore, our device demonstrates a larger operating bandwidth and higher tolerance to errors introduced during fabrication. Finally, we have also designed, fabricated and characterized a mode-converting PBS that not only separates the polarization states but also efficiently transforms the input power from a multimode waveguide to an output single-mode waveguide. The concept of free-form metamaterials demonstrated experimentally here can easily be applied to most photonic devices to drastically decrease their footprint without compromising their efficiency or functionality.

References

1. Manolatou, C. *et al.* High density integrated optics. *J. Lightw. Technol.* **17,** 1682–1692 (1999).
2. Fukuda, H. *et al.* Ultrasmall polarization splitter based on silicon wire waveguides. *Opt. Express* **14,** 12401–12408 (2006).
3. Yuan, W. *et al.* Mode-evolution-based polarization rotator-splitter design via simple fabrication process. *Opt. Express* **20,** 10163–10169 (2012).
4. Watts, M. R., Haus, H. A. & Ippen, E. P. Integrated mode-evolution-based polarization splitter. *Opt. Lett.* **30,** 967–969 (2005).
5. Hong, J. M. *et al.* Design and fabrication of a significantly shortened multimode interference coupler for polarization splitter application. *IEEE Photon. Technol. Lett.* **15,** 72–74 (2003).
6. Tu, Z. *et al.* A compact SOI polarization beam splitter based on multimode interference couple. *Proc. SPIE*, **8307**, 830707 (2011).
7. Dai, D., Wang, Z. & Bowers, J. E. Ultrashort broadband polarization beam splitter based on an asymmetrical directional coupler. *Opt. Lett.* **36,** 2590–2592 (2011).
8. Feng, J. & Zhou, Z. Polarization beam splitter using a binary blazed grating coupler. *Opt. Lett.* **32,** 1662–1664 (2007).
9. Yue, Y., Zhang, L., Yang, J.-Y., Beausoleil, R. G. & Willner, A. E. Silicon-on-insulator polarization splitter using two horizontally slotted waveguides. *Opt. Lett.* **35,** 1364–1366 (2010).
10. Kiyat, I., Aydinli, A. & Dagli, N. A compact silicon-on-insulator polarization splitter. *IEEE Photon. Technol. Lett.* **17,** 100–102 (2005).
11. Liu, T., Zakharian, A. R., Fallahi, M., Moloney, J. V. & Mansuripur, M. Design of a compact photonic-crystal-based polarizing beam splitter. *IEEE Photon. Technol. Lett.* **17,** 1435–1437 (2005).
12. Guan, X., Wu, H., Shi, Y., Wosinski, L. & Dai, D. Ultracompact and broadband polarization beam splitter utilizing the evanescent coupling between a hybrid plasmonic waveguide and a silicon nanowire. *Opt. Lett.* **38,** 3005–3008 (2013).
13. Sesay, M., Jin, X. & Ouyang, Z. Design of polarization beam splitter based on coupled rods in a square-lattice photonic crystal. *J. Opt. Soc. Am. B* **30,** 2043–2047 (2013).
14. Dai, D., Wang, Z., Peters, J. & Bowers, J. E. Compact polarization beam splitter using an asymmetrical Mach–Zehnder interferometer based on silicon-on-insulator waveguides. *IEEE Photon. Technol. Lett.* **24,** 673–675 (2012).
15. Soldano, L. B. *et al.* Mach–Zehnder interferometer polarization splitter in InGaAsP/InP. *IEEE Photon. Technol. Lett.* **6,** 402–405 (1994).
16. Lu, J. & Vučković, J. Nanophotonic computational design. *Opt. Express* **21,** 13351–13367 (2013).
17. Shen, B., Wang, P., Polson, R. & Menon, R. Integrated metamaterials for efficient and compact free-space-to-waveguide coupling. *Opt. Express* **22,** 27175–27182 (2014).
18. Piggott, A. Y. *et al.* Inverse design and implementation of a wavelength demultiplexing grating coupler. *Sci. Rep.* **4,** 7210 (2014).
19. Kim, G., Dominguez-Caballero, J.-A., Lee, H., Friedman, D. J. & Menon, R. Increased photovoltaic power output via diffractive spectrum separation. *Phys. Rev. Lett.* **110,** 123901 (2013).
20. Shen, B., Wang, P., Polson, R. & Menon, R. Ultra-high-efficiency metamaterial polarizer. *Optica* **1,** 356–360 (2014).
21. Wang, P. & Menon, R. Optimization of generalized dielectric nanostructures for enhanced light trapping in thin-film photovoltaics via boosting the local density of optical states. *Opt. Express* **22,** A99–A110 (2014).
22. Shen, B., Wang, P. & Menon, R. Optimization and analysis of 3D nanostructures for power-density enhancement in ultra-thin photovoltaics under oblique illumination. *Opt. Express* **22,** A311–A319 (2014).
23. Kim, G. & Menon, R. An ultra-small three dimensional computational microscope. *Appl. Phys. Lett.* **105,** 061114 (2014).
24. Oskooi, A. F. *et al.* MEEP: a flexible free-software package for electromagnetic simulations by the FDTD method. *Comput. Phys. Commun.* **181,** 687–702 (2010).
25. Liu, L., Ding, Y., Yvind, K. & Hvam, J. M. Efficient and compact TE–TM polarization converter built on silicon-on-insulator platform with a simple fabrication process. *Opt. Lett.* **36,** 1059–1061 (2011).
26. Bogaerts, W. *et al.* Basic structures for photonic integrated circuits in silicon-on-insulator. *Opt. Express* **12,** 1583–1591 (2004).

Author contributions

B.S., P.W. and R.M. conceived and designed the experiments. B.S., P.W. and R.P. contributed materials/analysis tools. B.S. performed the experiments. B.S., R.P. and R.M. analysed the data. B.S., R.P. and R.M. wrote the paper.

Additional information

Supplementary information is available in the online version of the paper. Reprints and permissions information is available online at www.nature.com/reprints. Correspondence and requests for materials should be addressed to R.M.